Machine-Learning-Powered EM-Based Framework for Efficient and Reliable Design of Low Scattering Metasurfaces

Slawomir Koziel, *Senior, Member, IEEE*, and Muhammad Abdullah

***Abstract*— Popularity of metasurfaces has been continuously growing due to their attractive properties including the ability to effectively manipulate electromagnetic (EM) waves. Metasurfaces comprise optimized geometries of unit cells arranged as a periodic lattice to obtain a desired EM response. One of their emerging application areas is the stealth technology, in particular, realization of radar cross section (RCS) reduction. Despite potential benefits, a practical obstacle hindering widespread metasurface utilization is the lack of systematic design procedures. Conventional approaches are largely intuition-inspired and demand heavy designer's interaction while exploring the parameter space and pursuing optimum unit cell geometries. Not surprisingly, these are unable to identify truly optimum solutions. In this article, we introduce a novel machine-learning-based framework for automated and computationally efficient design of metasurfaces realizing broadband RCS reduction. Our methodology is a three-stage procedure that involves global surrogate-assisted optimization of the unit cells, followed by their local refinement. The last stage is direct EM-driven maximization of the RCS reduction bandwidth, facilitated by appropriate formulation of the objective function involving regularization terms. The appealing feature of the proposed framework is that it optimizes the RCS reduction bandwidth directly at the level of the entire metasurface as opposed to merely optimizing unit cell geometries. Computational feasibility of the optimization process, especially its last stage, is ensured by high-quality initial designs rendered during the first two stages. To corroborate the utility of our procedure, it has been applied to several metasurface designs reported in the literature, leading to the RCS reduction bandwidth improvement by 15%–25% when compared with the original designs. Furthermore, it was used to design a novel metasurface featuring over 100% of relative bandwidth. Although the procedure has been used in the context of RCS design, it can be generalized to handle metasurface development for other application areas.**

***Index Terms*— Metasurface, machine learning, electromagnetic (EM)-driven design optimization, radar cross section (RCS), scattering manipulation.**

I. Introduction

METASURFACES are planar patterned surfaces composed of subwavelength periodic arrays of unit cells [1]. Within the past decade, their unique ability to manipulate the wavefront fostered utilization in many important applications, for example, beam-switching antennas, polarization converters, invisibility cloaks, gradient index lenses, holograms, stealth technology, and many others [2]–[6]. In the stealth technology, the main bottleneck is to reduce the radar cross section (RCS) to avoid detection by the enemy's radar. This can be accomplished by minimizing the backscattered electromagnetic (EM) energy from the metallic objects [7]. Some of the techniques implemented to accomplish RCS reduction include object reshaping method [8], invisibility cloaking [9], using radar absorbing materials (RAMs) [10], and active and passive cancellation [9]. Nevertheless, the downsides of the aforesaid techniques are narrow RCS reduction bandwidth, structural complexity, and severe losses.

An alternative approach to reduce the backscattered EM energy is to replace the conventional metallic surface with artificially engineered materials (metamaterials). The two prominent design strategies in this regard are to use metamaterials as an absorber [11]–[14] or to exploit their distinctive property of manipulating the phase reflection characteristics. In the former case, the incident EM energy transforms into heat; hence, backscattering energy can be diminished. Notwithstanding, the RCS reduction bandwidth still remains limited. The latter involves a periodic combination of artificial magnetic conductors (AMCs), and perfect electric conductors (PECs), arranged to attain the desired phase reflection characteristics. Two types of structures have been proposed that capitalize on this concept, that is, the EM gradient surface (EGS) [15] and the checkerboard metasurface [6]. In EGS, the metallic portion of the surface is substituted by the periodic arrays of AMC and PEC cells. When the plane wave is incident from the normal direction, the backscattered energy is tilted from that direction, thereby reducing the RCS. The fundamental condition in EGS is to maintain equal phase difference between the AMC and PEC unit cells [16]. The nonlinear relationship between the phase reflection characteristics and

Manuscript received October 28, 2020; revised December 18, 2020; accepted January 26, 2021. Date of publication March 8, 2021; date of current version April 2, 2021. This work was supported in part by the Icelandic Centre for Research (RANNIS) under Grant 206606051 and in part by the National Science Centre of Poland under Grant 2018/31/B/ST7/02369. *(Corresponding author: Muhammad Abdullah.)*

Slawomir Koziel is with the Engineering Optimization and Modeling Center, Reykjavik University, 101 Reykjavik, Iceland, and also with the Faculty of Electronics, Telecommunications and Informatics, Gdańsk University of Technology, 80-233 Gdańsk, Poland (e-mail: koziel@ru.is).

Muhammad Abdullah is with the Engineering Optimization and Modeling Center, Reykjavik University, 101 Reykjavik, Iceland (e-mail: muhammada19@ru.is).

Color versions of one or more figures in this article are available at https://doi.org/10.1109/TMTT.2021.3061128.

Digital Object Identifier 10.1109/TMTT.2021.3061128

frequency poses considerable challenges in satisfying the equal phase difference requirement over a wide frequency band. In the case of a checkerboard metasurface, the AMC and PEC cells are organized in an alternate fashion, and the objective is to maintain 180° phase difference between the AMC and PEC cells. By doing so, the incident EM energy scatters at four lobes in the diagonal plane [17], leading to low scattering property of the surface. The main advantages of the aforementioned surfaces include structural simplicity, robustness, and low profile [18]. However, the AMC structure exhibits relatively narrowband characteristics; outside the operating bandwidth, it starts resembling PEC. Consequently, the 180° phase difference condition no longer holds. To tackle this situation, de Cos *et al.* [19], [20] suggested utilization of two AMC cells instead of one to realize a dual resonance structure [21], [22]. The PEC unit cells are replaced by an additional AMC cell operating at a different resonant frequency. When exploiting such a structure to accomplish RCS reduction over a broad frequency band, the phase difference between the two AMC cells should remain 180° while retaining their reflection amplitudes identical and equal to 1 [17], [23]. In other words, the phase reflection curves of a pair of unit cells should remain equidistant over the frequency band where RCS reduction is to be achieved. Due to the presence of ohmic and tangent losses, the reflection amplitudes of the combined unit cells are not precisely the same. Therefore, it has been established that –10-dB RCS reduction can be maintained over a frequency band if the phase difference between the two AMC cells remains within the 143°–217° range (i.e., 180°± 37°) [24]. More recently, the concepts of coding metasurfaces [25], diffusion metasurfaces [26], [27], programmable metasurfaces [30], Huygens' metasurfaces [31], and cloaking structures [32] have been proposed, which offer a control over the wavefront in a more sophisticated manner. The primary advantage of coding and diffusion metasurfaces over the checkerboard type surfaces is that it scatters the incident EM waves into all directions. In addition, coding metasurfaces are also being exploited as an absorptive surface to realize essential RCS reduction [33].

To date, many metasurface architectures have been proposed to accomplish wideband RCS reduction [17], [19]–[29]. Due to the lack of reliable theoretical models, the conventional design methodologies mostly rely on empirical reasoning, physical intuition, or trial and error. Additionally, a considerable involvement of human interaction makes such methods laborious and time-consuming, also because full-wave EM simulations have to be used to evaluate metasurface characteristics in a reliable manner. Altogether, the aforementioned downsides pose serious questions concerning the efficacy of experience-driven methods, and their capability of finding truly optimum designs. Considering the practical design measures, the problem is additionally exacerbated by highly nonlinear input–output relationships. Efficient development of high-performance metasurfaces requires a new algorithmic framework that goes beyond interactive approaches and permits design automation, reliability, and computational efficiency. At this point, it should be mentioned that unprecedented advancements in computing hardware and software considerably increased the popularity and widespread use of rigorous EM-driven design methodologies, primarily based on numerical optimization [34]. However, direct EM optimization of metasurface designs when using conventional algorithms may be prohibitively expensive, especially when global search is required. A practical workaround is utilization of machine learning methods [35]–[39], including surrogate modeling techniques [41]–[44]. Shifting the computational burden to a cheaper representation of the structure at hand and the incorporation of other means such as problem decomposition [45] may expedite the parameter tuning process and enable globalized search, otherwise infeasible when operating directly on EM simulation models. At this point, it should be mentioned that more generic approaches are also possible, where parametric optimization of the unit cells (and the metasurface) of a fixed geometry is replaced by topology optimization. In this case, the entire geometry of the metasurface is subject to the optimization process, which brings in additional degrees of freedom. This type of tasks is often handled using inverse modeling methods (see [46], [47]).

This article describes a rigorous machine-learning-based framework for efficient EM-driven design of low scattering metasurfaces. Its basic components include surrogate modeling of AMC cells and their concurrent optimization using a combination of global search and local refinement, as well as direct local tuning of the entire metasurface. Utilization of surrogate models allows for expediting the process of parameter adjustment that aims at broadening the frequency range for which the phase difference between two AMC cells remains within the 143°–217° range. Having optimum unit cell geometries, further EM-driven tuning of the cell parameters is carried out at the level of the entire checkerboard metasurface. The process is fast due to the availability of a good initial design produced at the earlier stages, as well as utilization of trust-region (TR) gradient algorithm with sparse sensitivity updates [45]. Moreover, a regularization approach is used to efficiently handle frequency-localized violations of the RCS reduction threshold that occur while enhancing the overall reduction bandwidth. To calculate the RCS reduction bandwidth of a metasurface, a PEC surface of a similar size is implemented to be used as a reference surface. In this study, we considered checkerboard metasurfaces to demonstrate the utility our framework; nevertheless, the introduced design optimization methodology is not limited to this particular class of structures. The presented procedure is generic and can be applied to any type of metasurface architecture. At the same time, it should be emphasized that the proposed optimization procedure addresses the problem of parameter adjustments of unit cells and metasurfaces of fixed geometry. Topology optimization is outside the scope of this work.

The presented framework addresses the key challenges of metasurface design as elaborated on earlier in this section. It enables fully automated and optimum design within the assumed parameter space. The design methodology is validated both numerically and experimentally. The technical novelty and major contributions of this article can be summarized as follows: 1) the development of machine-learning-powered framework for reliable and efficient EM-based optimization of checkerboard metasurfaces; 2) demonstrating the practical

utility of our approach in the context of broadband metasurface design using three application examples; and 3) the development of a high-performance checkerboard metasurface featuring over 100% relative RCS reduction bandwidth. To the authors' knowledge, the proposed framework is the first systematic procedure proposed in the literature for globally optimum design of low scattering checkerboard metasurfaces.

The remaining part of the article is organized as follows. In Section II, we formulate the metamodeling-based procedure for concurrent optimization of the pairs of unit cell geometries. Subsequently, a regularization-based formulation of the metasurface design problem is provided for broadband RCS reduction, followed by a complete optimization procedure. In Section III, we demonstrate the performance of the proposed procedure using three benchmark examples. Section IV provides experimental validation of the metasurface design featuring over 100% RCS reduction bandwidth. Section V concludes the article.

II. Machine-Learning-Powered EM-Based Metasurface Design

This section provides a comprehensive description of the proposed machine-learning-powered EM-driven design procedure. We start by presenting the metamodel-based procedure for concurrent optimization of the pairs of unit cells for required reflection phase characteristics. Subsequently, a regularization-based formulation of the metasurface design problem is provided for broadband RCS reduction. The section is concluded with a summary of a complete optimization procedure. Application of the proposed framework to low scattering metasurface design will be provided in Section III.

A. Concurrent Unit Cell Optimization by Machine Learning

The purpose of the machine-learning-based optimization procedure is to find a pair of unit cell designs featuring the phase difference within the range of $180^\circ \pm \alpha_{\max}$ over a possibly broad frequency range F. Here, $\alpha_{\max}$ is set to 37°, as suggested in [24]. The vectors of designable variables for a pair of unit cells will be denoted as $\boldsymbol{x}_1 = [x_{1.1} \ldots x_{1.n}]^T \in X_1$ and $\boldsymbol{x}_2 = [x_{2.1} \ldots x_{2.n}]^T \in X_2$, and their EM simulated responses will be represented by $\boldsymbol{P}_1(\boldsymbol{x})$ and $\boldsymbol{P}_2(\boldsymbol{x})$, respectively. The latter denotes the phase reflection characteristics. The parameter space X_i is determined by the user-defined lower and upper bounds $\boldsymbol{l}_i = [l_{i.1} \ldots l_{i.n}]^T$ and $\boldsymbol{u}_i = [u_{i.1} \ldots u_{i.n}]^T$ so that $l_{i.l} \le x_{i.l} \le u_{i.l}$, $l = 1,\ldots, n$ and $i = 1, 2$. Notwithstanding, in many practical cases, the topology and hence the vector of designable variables for the two unit cells is identical.

Initially, the acquisition of the training data is carried out by uniformly allocating N samples within the parameter spaces, X_1 and X_2, and evaluating the EM simulation model to obtain the corresponding responses. Subsequently, the metamodels $\boldsymbol{S}_1$ and $\boldsymbol{S}_2$ are constructed within X_1 and X_2 using kriging interpolation [40], [41]. The model is trained using the data samples $\{\boldsymbol{x}_i^{(k)}, \boldsymbol{P}_i\ (\boldsymbol{x}_i^{(k)})\}_{k=1,\ldots,Ni}$, where $\boldsymbol{P}_i(\boldsymbol{x}_i^{(k)})$ and N_i denotes the EM-simulated response of the kth design and the total number of training samples for the ith unit cell, respectively. The data samples are arranged on a rectangular grid, which is a suitable design of experiment strategy for a low-dimensional case. The allocation of the grid nodes in each direction is decided based on the large-scale sensitivity analysis.

Kriging is a Gaussian process-based modeling technique [40] widely used for constructing interpolating surrogates in a broad range of applications. For the convenience of the reader, a brief outline of the technique is provided below assuming scalar output. Generalization for vector-valued functions is straightforward. The function of interest is assumed to be of the form

$$f(\boldsymbol{x}) = \boldsymbol{g}(\boldsymbol{x})^T \boldsymbol{\beta} + Z(\boldsymbol{x}) \tag{1}$$

where $\boldsymbol{g}(\boldsymbol{x}) = [g_1(\boldsymbol{x})\ g_2(\boldsymbol{x}) \ldots g_N(\boldsymbol{x})]^T$ are known (here, EM-simulated) system responses, $\boldsymbol{\beta} = [\beta_1 \beta_2 \ldots \beta_N]^T$ are the unknown hyperparameters, and $Z(\boldsymbol{x})$ is a realization of a normally distributed Gaussian random process with zero mean and variance σ^2. The regression component $\boldsymbol{g}(\boldsymbol{x})^T\ \boldsymbol{\beta}$ serves as a trend function for f, whereas $Z(\boldsymbol{x})$ manages localized variations from the trend. The covariance matrix of $Z(\boldsymbol{x})$ is

$$Cov\left[Z\left(\boldsymbol{x}^{(i)}\right) Z\left(\boldsymbol{x}^{(j)}\right)\right] = \sigma^2 \boldsymbol{R}\left(\left[R\left(\boldsymbol{x}^{(i)}, \boldsymbol{x}^{(j)}\right)\right]\right) \tag{2}$$

where $\boldsymbol{R}$ is a $p \times p$ correlation matrix with $R_{ij} = R(\boldsymbol{x}^{(i)}, \boldsymbol{x}^{(j)})$, and $R(\boldsymbol{x}^{(i)}, \boldsymbol{x}^{(j)})$ is the correlation function between data samples $\boldsymbol{x}^{(i)}$ and $\boldsymbol{x}^{(j)}$. Here, we use a Gaussian correlation function of the form

$$R(\boldsymbol{x}, \boldsymbol{y}) = \exp\left[-\sum_{k=1}^{n} \theta_k |x_k - y_k|^2\right] \tag{3}$$

where θ_k are the unknown correlation parameters, and x_k and y_k are the kth elements of the vectors $\boldsymbol{x}$ and $\boldsymbol{y}$, respectively. The kriging model is defined as [40]

$$\boldsymbol{s}(\boldsymbol{x}) = \boldsymbol{g}(\boldsymbol{x})^T \boldsymbol{\beta} + \boldsymbol{r}^T(\boldsymbol{x}) \boldsymbol{R}^{-1} (\boldsymbol{h} - \boldsymbol{G}\boldsymbol{\beta}) \tag{4}$$

where

$$\boldsymbol{r}(\boldsymbol{x}) = \left[R\left(\boldsymbol{x}, \boldsymbol{x}^{(1)}\right) \ldots R\left(\boldsymbol{x}, \boldsymbol{x}^{(p)}\right)\right] \tag{5}$$

$$\boldsymbol{f} = \left[f\left(\boldsymbol{x}^{(1)}\right) f\left(\boldsymbol{x}^{(2)}\right) \ldots f\left(\boldsymbol{x}^{(p)}\right)\right]^T \tag{6}$$

and $\boldsymbol{G}$ is a $p \times N$ matrix with $G_{ij} = P_j(\boldsymbol{x}^{(i)})$. The vector of model parameters $\boldsymbol{\beta}$ can be computed as

$$\boldsymbol{\beta} = \left(\boldsymbol{G}^T \boldsymbol{R}^{-1} \boldsymbol{G}\right)^{-1} \boldsymbol{G}^T \boldsymbol{R}^{-1} \boldsymbol{f}. \tag{7}$$

Finally, model fitting is accomplished by maximum likelihood scheme for θ_k

$$-\left[p \ln\left(\sigma^2\right) + \ln |\boldsymbol{R}|\right]/2. \tag{8}$$

Here, both σ^2 and $\boldsymbol{R}$ are the functions of θ_k. The components of the vector-valued metamodels $\boldsymbol{S}_1$ and $\boldsymbol{S}_2$ of the phase characteristics $\boldsymbol{P}_1$ and $\boldsymbol{P}_2$, respectively, are the kriging interpolation surrogates rendered for phase responses at all individual frequencies in the considered frequency sweep.

Having the trained metamodels $\boldsymbol{S}_1$ and $\boldsymbol{S}_2$, the concurrent unit cell optimization is carried out over the joint parameter space of the pair of cells, that is, the Cartesian product $X_1 \times X_2$. The goal of the optimization procedure is to find a pair of unit cell designs $\boldsymbol{x}_p^* = [(\boldsymbol{x}_1^*)^T\ (\boldsymbol{x}_2^*)^T]^T$ maximizing the frequency

range for which the phase difference between the two satisfies the condition

$$180^\circ - \alpha_{\max} \le \Delta\boldsymbol{P}\left(\left[\left(\boldsymbol{x}_1^*\right)^T \left(\boldsymbol{x}_2^*\right)^T\right]^T\right) \le 180^\circ + \alpha_{\max}. \quad (9)$$

Specifically, the design task can be formulated as follows:

$$\boldsymbol{x}_p^* = \arg\min_{\boldsymbol{x}_p \in X_1 \times X_2} U\left(\Delta\boldsymbol{P}\left(\boldsymbol{x}_p\right)\right) \quad (10)$$

and the objective function U is defined as

$$U\left(\Delta\boldsymbol{P}\left(\boldsymbol{x}_p\right)\right) = -\left[f_R\left(\boldsymbol{x}_p\right) - f_L\left(\boldsymbol{x}_p\right)\right] \quad (11)$$

where f_L and f_R are the frequencies defining the largest continuous frequency range for which condition (9) is satisfied. The minus sign in (11) turns the maximization task into the minimization one.

Global optimization is performed based on a structured grid (in an exhaustive manner). Let $M_{m1\ldots mn}$ be a rectangular grid such that $\boldsymbol{x}_i \in M_{i.m1\ldots mn}$ if and only if $\boldsymbol{x}_i = [x_{i.1}\ldots x_{i.n}]^T$ is of the form $x_{i.k} = l_{i.k} + j_{i.k}[(u_{i.k}–l_{i.k})/m_{i.k}]$, $k = 1,\ldots, n$, and $i = 1, 2$, where $m_{i.k}$ is a grid-defining integer for the kth variable of ith unit cell, and $j_{i.k} \in \{0, 1,\ldots, m_{i.k}\}$. The initial approximation $\boldsymbol{x}_p^{(0)}$ of the global optimum of $\boldsymbol{S}_1$ and $\boldsymbol{S}_2$ is found as

$$\boldsymbol{x}_p^{(0)} = \arg\min_{\substack{\boldsymbol{x}_1 \in M_{1.m_1\ldots m_n} \\ \boldsymbol{x}_2 \in M_{2.m_1\ldots m_n}}} U\left(\Delta\boldsymbol{P}\left(\left[\left(\boldsymbol{x}_1\right)^T \left(\boldsymbol{x}_2\right)^T\right]\right)\right). \quad (12)$$

In other words, $\boldsymbol{x}_p^{(0)}$ is obtained by exploring all possible combinations of unit cell designs $\boldsymbol{x}_1 \in M_{1.m1\ldots mn}$ and $\boldsymbol{x}_2 \in M_{2.m1\ldots mn}$ and identifying the one that minimizes U. After determining $\boldsymbol{x}_p^{(0)}$, the local refinement is executed using gradient-based search [48]. The computational cost of the global and local optimization process is negligible because it is executed at the level of the fast kriging metamodels $\boldsymbol{S}_1$ and $\boldsymbol{S}_2$. Additionally, the complete procedure is implemented in a vectorized manner to further speed-up its operation. Clearly, there is an initial cost associated with the acquisition of the training data for surrogate model construction. The latter is unavoidable to render the aforementioned computational benefits and to enable global search in the first place. The details concerning the acquisition cost are provided in Section III in the context of specific verification examples considered therein.

B. EM-Driven Metasurface Refinement for RCS Reduction Bandwidth Enhancement

Upon adjusting the unit cell parameters as described in Section II-A, EM-driven refinement of the entire metasurface is carried out. This stage is necessary because optimized dimensions of the cells do not translate into optimum design of the entire structure; recall that the unit cells were tuned to satisfy the phase condition (9). To obtain the best possible performance, the enhancement of the RCS bandwidth has to be performed directly.

Let $\boldsymbol{x}_A$ denote the aggregated $(n_1 + n_2)\times$ 1 geometrical parameter vector of the pair of the unit cells. Furthermore, let $\boldsymbol{R}_{\text{red}}(\boldsymbol{x}_A, f)$ represent the frequency characteristics representing the RCS reduction, that is, the difference between the monostatic RCS of a reference (metallic) surface and that of the considered metasurface, where f stands for the frequency. Conventionally, the RCS reduction bandwidth B_{RCS} to be maximized is defined as the broadest continuous frequency range satisfying the condition $\boldsymbol{R}_{\text{red}}(\boldsymbol{x}_A, f) \ge r_{\max}$, where $r_{\max}$ stands for the acceptance threshold (e.g., 6 or 10 dB).

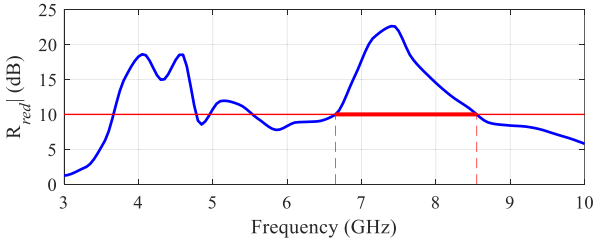

Fig. 1. Exemplary RCS reduction characteristics with the RCS bandwidth marked using the thick horizontal line and representing the largest (continuous) frequency range satisfying the condition $\boldsymbol{R}_{\text{red}}(\boldsymbol{x}_A, f) \ge r_{\max}$; here, $r_{\max} = 10$ dB.

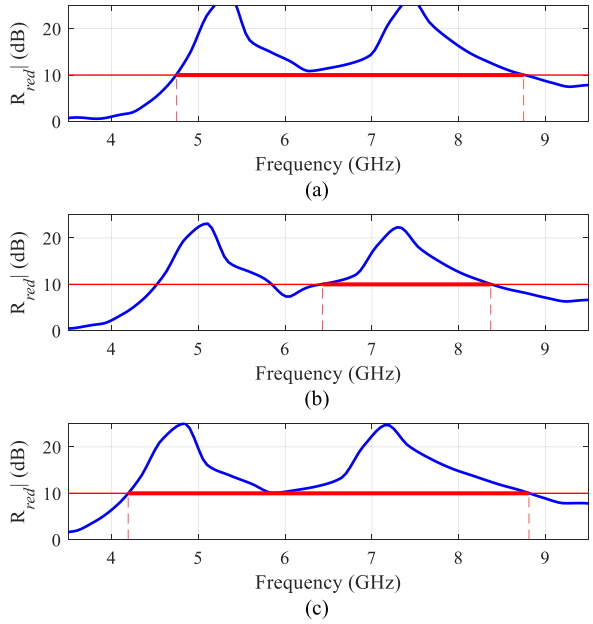

Fig. 2. Practical issues related to conventional RCS bandwidth reduction definition. The sequence of plots from (a) to (c) indicates RCS characteristics at (a) initial design, (b) intermediate design, and (c) optimum design featuring the largest bandwidth. Because the intermediate design exhibits violation of the $r_{\max}$ threshold, the bandwidth at this design is significantly smaller than around the initial design and the optimum design. In other words, a discontinuity occurs, which can make the optimum design unattainable from the given initial design when using local optimization routine (the only practical option for direct EM-driven metasurface design).

This is illustrated in Fig. 1. The problem with this definition has been indicated in Fig. 2. If the initial and the optimum design are separated by the designs that violate the acceptance threshold $r_{\max}$ [see Fig. 2(b)], a discontinuity of the bandwidth value will be observed along the path connecting the two designs, which essentially prevents local (e.g., gradient-based) optimization algorithm from reaching the optimum.

The latter is the only practical option for direct EM-driven metasurface tuning due to high costs incurred by structure evaluation. On the other hand, a situation as illustrated in Fig. 2

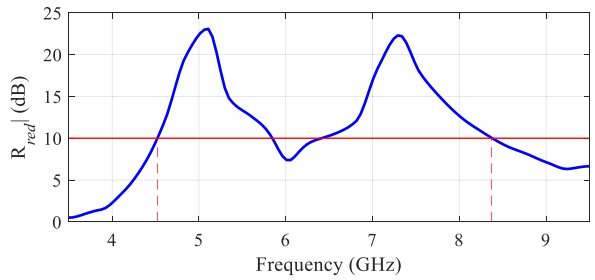

Fig. 3. Exemplary RCS characteristic with the lower frequency f_L, upper frequency f_H, and $r_{\max}$ violation d_r marked to indicate the defining quantities of the objective function for RCS reduction bandwidth improvement.

is a commonplace because the optimum design would often correspond to the RCS characteristics almost violating the threshold at certain frequencies [see Fig. 2(c)]. Consequently, an efficient adjustment of metasurface parameters needs a different formulation of the objective function.

Consider Fig. 3, where the frequencies f_L and f_H stand for the minimum and the maximum frequencies (within the considered simulation range) for which the condition $\boldsymbol{R}_{\text{red}}(\boldsymbol{x}_A, f) \geq r_{\max}$ is satisfied. Let d_r stand for the maximum violation of the above condition within the frequency interval $[f_L\, f_H]$. Using these, the objective function U_{RCS} for metasuface tuning will be defined as

$$U_{\text{RCS}}(\boldsymbol{x}_A) = -[f_H(\boldsymbol{x}_A) - f_L(\boldsymbol{x}_A)] + \beta c_r(\boldsymbol{x}_A)^2. \quad (13)$$

The first term in (5) is the negative RCS reduction bandwidth (to turn the task into a minimization problem). The second component is a regularization term with the function c_r defined as $c_r(\boldsymbol{x}_A) = d_r$ if $d_r > 0$ and zero otherwise. Its purpose is to increase the objective function if violation of the acceptance threshold is detected.

The contribution of the regularization term is controlled by coefficient β. Here, it is set to $\beta = 1$, but this value is not critical. Nevertheless, it can be used to control the amount of violation that can be tolerated.

The most important advantage of formulation (13) is that is effectively alleviates the difficulty related to conventional formulation. In particular, the objective function does not exhibit discontinuities related to in-band violation of the acceptance threshold, which makes the optimum design attainable through local search for situations depicted in Fig. 2.

The optimization process is realized using the TR gradient search algorithm [48], [50]. The parameter tuning task is formulated as

$$\boldsymbol{x}_A^* = \arg \min_{\boldsymbol{x}_A \in X_1 \times X_2} U_{\text{RCS}}(\boldsymbol{x}_A). \quad (14)$$

The TR algorithm renders a series of approximations $\boldsymbol{x}_A^{(j)}$, $j = 0, 1, \ldots$, to $\boldsymbol{x}_A^*$ as

$$\boldsymbol{x}_A^{(j+1)} = \arg \min_{\substack{\boldsymbol{x} \in X_1 \times X_2 \\ \boldsymbol{x}_A^{(j)} - \boldsymbol{d}^{(j)} \leq \boldsymbol{x}_A \leq \boldsymbol{x}_A^{(j)} - \boldsymbol{d}^{(j)}}} L_{\text{RCS}}^{(j)}(\boldsymbol{x}_A) \quad (15)$$

where $L_{\text{RCS}}^{(j)}$ is the objective function of the form of (13) but computed from the first-order Taylor expansion model of $\boldsymbol{R}_{\text{red}}(\boldsymbol{x}_A, f)$ established at the current iteration point $\boldsymbol{x}_A^{(j)}$.

The construction of the Taylor model requires the knowledge of the Jacobian matrix of $\boldsymbol{R}_{\text{red}}$, which is estimated using finite differentiation in the first iteration and then updated by the adaptive application of the rank-one Broyden formula [45]. Using this approach, the tuning process can be realized at a low computational cost, typically about $M \cdot n$ of EM simulations of the metasurface, where n is the number of geometrical parameters, and $M = 3$–4. The TR size vector $\boldsymbol{d}^{(j)}$ is adjusted by means of the standard TR rules [48].

C. Optimization Framework

The algorithm starts by defining the lower and upper bounds to determine the parameter spaces X_i and allocating N_i samples. The rectangular grids M_i (see Section II-A) are established by investigating the large-scale sensitivities of the unit cell responses to their geometrical parameters. The training data are obtained by evaluating the EM simulation model at the assigned locations. In the next step, the kriging metamodels $\boldsymbol{S}_1$ and $\boldsymbol{S}_2$ are constructed and used as predictors of a unit cell reflection phase characteristics over the spaces X_i. The concurrent unit cell optimization is then carried out to find a pair of cell designs featuring the phase difference within a particular range.

The first stage of this process is a global search (4), followed by local (gradient-based) tuning. Having the optimum pair of unit cells, their periodic arrays are used in an alternate manner to characterize a checkerboard metasurface. Finally, EM-driven fine tuning of the cell parameters is carried out at the level of the entire surface. This stage follows the procedure described in detail in Section II-B.

The proposed framework enables expedited and efficient development of high-performance metasurfaces featuring broadband RCS reduction characteristics. The flow diagram of the machine-learning-powered EM-based design framework has been shown in Fig. 4, whereas Fig. 5 shows the flow diagram of the local tuning procedure.

III. Application Examples

This section presents the operation and performance of the machine-learning-powered EM-based design procedure using three application case studies. We start by applying the proposed framework to a geometrically simple structure. This example is also used to explain and emphasize the importance of various components of the algorithmic procedure. Subsequently, two more cases are considered featuring more complex unit cell geometries. The obtained RCS reduction bandwidths are compared with those reported in the source article. A discussion of the results and various aspects of the presented framework is also provided in the last part of this section. The experimental validation of one of the considered metasurfaces will be discussed in Section IV.

A. Case 1: Checkerboard EBG Surface Utilizing Rectangular and Circular Cell Topologies

Our first application example is a checkerboard surface consisting of a rectangular and circular shape unit cells. The

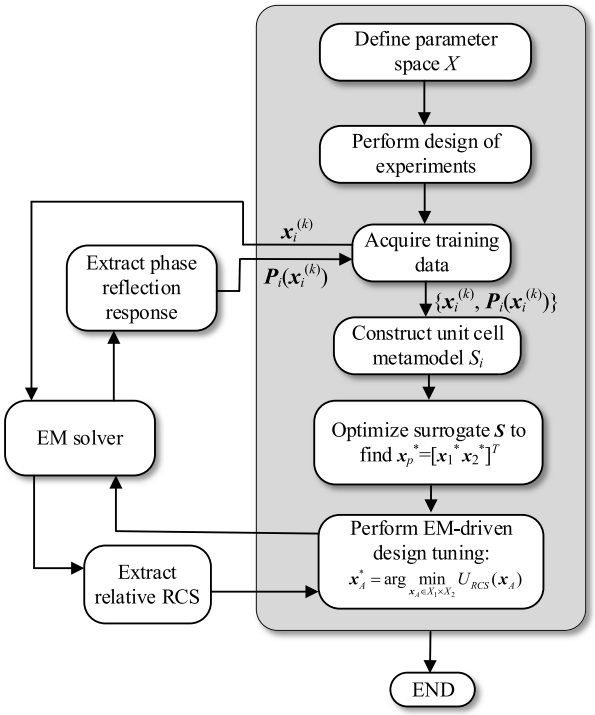

Fig. 4. Flow diagram of the proposed machine-learning-powered EM-based framework for developing low scattering metasurfaces.

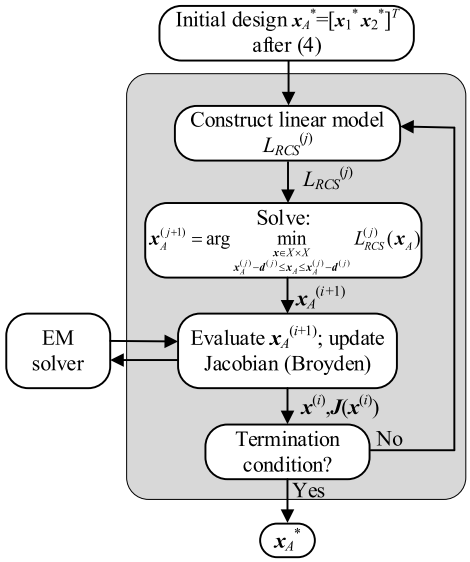

Fig. 5. Flow diagram of the EM-based local refinement stage.

cell geometries and the entire surface configuration are shown in Figs. 6 and 8, respectively. The structure is based on a design proposed in [23]. It is implemented on a ground-backed Rogers RT/duroid 5880 lossy substrate ($\varepsilon_r = 2.2$, $h = 6.35$ mm, $\tan\delta = 0.0009$). During the simulations, metallization is represented as perfect electrical conductor (PEC). The overall size of a single unit cell is $W_s \times L_s = 15 \times 15$ mm^2. As shown in Fig. 6, there are two geometrical parameters l and w, for Cell 1, and one parameter d for Cell 2 that control the design topology of a corresponding unit cell.

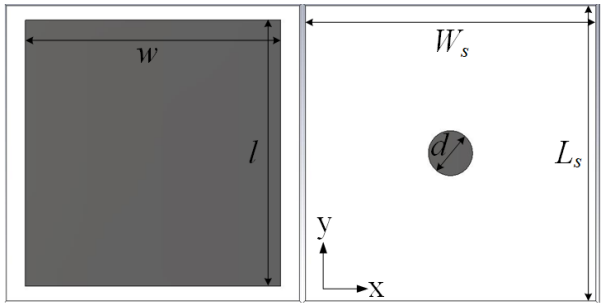

Fig. 6. Geometries of the optimized unit cell designs: Cell 1 (left), and Cell 2 (right).

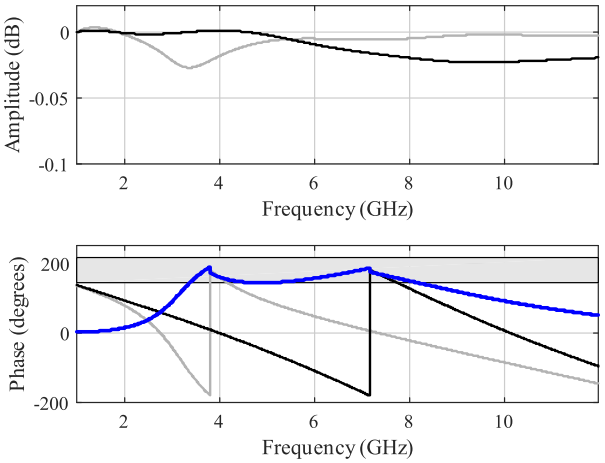

Fig. 7. Reflection performance of the optimized unit cells: reflection amplitude (top) and reflection phase (bottom). The responses of Cell 1 and Cell 2 are marked gray and black, respectively, whereas the blue curve indicates the reflection phase difference. The gray-shaded area in the bottom plot indicates the range of acceptable phase differences.

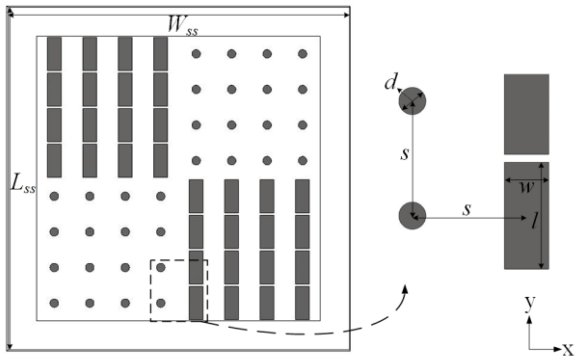

Fig. 8. Geometry configuration of the optimized metasurface (after three-stage optimization procedure).

Hence, the vectors of designable variables are $\boldsymbol{x}_1 = [l\ w]^T$ and $\boldsymbol{x}_2 = [d]^T$; L_s, W_s, W_{ss}, L_{ss}, and s are all fixed. The sample spaces X_1 and X_2 are defined by the lower and upper bounds as: $\boldsymbol{l}_1 = [12\ 12]^T$, $\boldsymbol{u}_1 = [14.9\ 14.9]^T$, and $\boldsymbol{l_2} = 1$, $\boldsymbol{u}_2 = 5$; all dimensions are in millimeters.

For constructing metamodels $\boldsymbol{S}_1$ and $\boldsymbol{S}_2$, the training points are arranged in a uniform grid $M_{14.14}$ and M_{100} (see Section II-A) with a total of 196 and 100 samples in the sample

spaces X_1 and X_2, respectively. A joint parameter space is the Cartesian product $X_1 \times X_2$. The acquired data are divided into the training (85%) and the test data (15%) to be used for split-sample error estimation. The frequency-domain solver of the CST Microwave Studio is used to evaluate the phase reflection responses of the unit cell.

The trained metamodels have been used at the concurrent unit cell optimization stages (procedure of Section II-A) to find the pair of designs, and the optimal geometries obtained in the process are $\boldsymbol{x}_1^* = [13.5263, 13.0684]^T$ and $\boldsymbol{x}_2^* = 2.2814$. Their topologies are shown in Fig. 6, and the EM-simulated reflection response along with the reflection phase difference between the two cells are presented in Fig. 7. It can be observed that condition (1) is satisfied for the continuous range of frequencies from 3.6 to 8.2 GHz, and hence the latter can be anticipated as the approximate RCS reduction bandwidth of the entire metasurface.

Having the optimal pair of unit cell designs, their periodic arrays are implemented in an alternate manner to characterize a 2×2 checkerboard metasurface; see Fig. 8. Each lattice of a periodic surface comprises 16 elements, that is, 4×4 planar array of Cell 1 or Cell 2. The total size of the surface is $W_{ss} \times L_{ss} = 120 \times 120$ mm^2. The interelement spacing of individual unit cells in an array is $s = 15$ mm. Again, the surface is implemented on a Rogers RT/duroid 5880 lossy substrate. To characterize the RCS reduction performance, a PEC surface of a similar size is also used. Hereafter, the EM-driven approach (see Section II-B) is adopted to fine-tune the RCS reduction bandwidth in the vicinity of the optimal cell geometries, following their surrogate-assisted global optimization and local refinement. To this end, the time-domain solver of CST Microwave Studio, MATLAB R2018a, and MATLAB-to-CST socket (for communication with the EM solver) is used.

To obtain the best possible performance, the optimization of the RCS reduction bandwidth has to be performed at the level of the entire metasurface. The availability of a good starting point, identified earlier, is critical to ensure reliability of the tuning process. In particular, it makes the utilization of the gradient-based algorithm sufficient to find a global optimum with a high likelihood. This is due to optimizing the unit cells in a global sense and the fact that the properties of the phase difference characteristics are good estimators of the RCS reduction bandwidth at the metasurface level. At the same time, utilization of the local optimization algorithm with its low computational cost is the only practical option when optimizing the EM model of the entire structure.

The optimum design obtained after the completion of the procedure given in Section II-B is $\boldsymbol{x}_A^* = [13.952, 5.824, 3.151]^T$. To corroborate the utility of a proposed design framework in the context of broadband RCS reduction, the monostatic RCS performance for the normal incidence has been determined. For the sake of comparison, the RCS performance reported in [23], the RCS reduction bandwidth obtained after designing the surface based on the optimum geometries identified after the procedure of Section II-A, and the final RCS characteristic upon accomplishing the metasurface optimization are all gathered in Fig. 9. It can be observed that

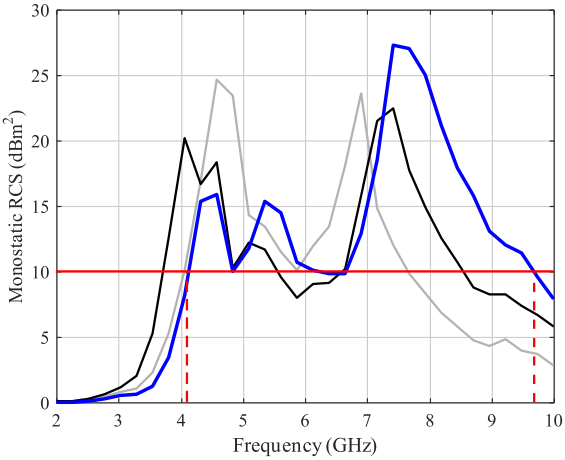

Fig. 9. Monostatic RCS performance of the metasurface design reported in [23] (gray), performance after the first and the second optimization stages (Section II-A) (black), and the performance of the final design (Section II-B) (blue). The horizontal red line represents the 10-dB RCS reduction threshold relative to the PEC surface.

the machine-learning-based concurrent unit cell optimization considerably increases the bandwidth compared with the conventional design approach. The EM-driven optimization of the entire structure further extends the RCS reduction bandwidth. It should be noted that the violation of the 10-dB threshold occurring at certain frequencies upon metamodeling-assisted cell optimization is efficiently handled by the TR algorithm. The 10-dB RCS reduction bandwidth at the final design extends from 4.1 to 9.7 GHz. This result corroborates the importance of EM-driven optimization at the metasurface level and demonstrates the efficacy of the methodology proposed in this work. The computational cost of the first and the second stage (machine-learning-powered unit cell optimization) is negligible, whereas the cost of EM-driven refinement stage is 15 metasurface simulations.

Throughout this work, Intel Xeon E5540 dual-core machine with 18-GB RAM is used. The EM simulation model of the unit cell and the entire surface contains about 19 000 and 563 000 mesh cells, respectively. The simulation time of the unit cell and the metasurface is about 40 s and 2 min, respectively. The CPU time required for training data acquisition is about 3 h, whereas the time required for the refinement stage is 30 min. As mentioned before, the cost of global and local optimization of the unit cells (conducted at the level of the kriging surrogate) is negligible. Consequently, the overall CPU time of the entire design optimization procedure is about 3 h 30 min.

The bistatic RCS performance versus the elevation angle theta θ along the principal and the diagonal planes is shown in Fig. 10. The results demonstrate that the metasurface exhibits more than the 15-dB RCS reduction in the principal and the diagonal planes, compared with the metallic surface. This reduction occurs because the reflected fields are redirected into four main lobes, instead of the single main lobe in the case of the metallic surface.

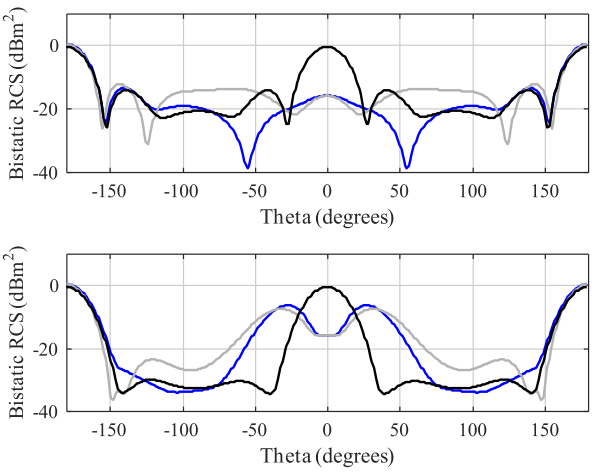

Fig. 10. Bistatic RCS performance at 5.5 GHz along the principal planes (top) and along the diagonal planes (bottom). The curves corresponding to the two planes $\varphi = 0/45$ and $\varphi = 90/135$ are marked in blue and gray, respectively, whereas the black curve indicates the scattered field from the PEC surface.

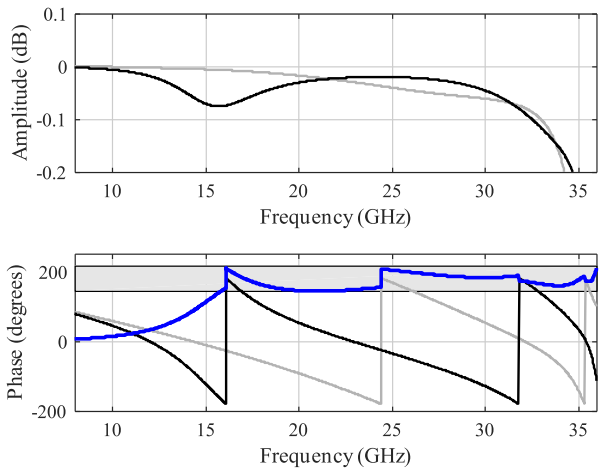

Fig. 12. Reflection performance of the optimized unit cells: reflection amplitude (top) and reflection phase (bottom). The responses of Cell 1 and Cell 2 are marked in black and gray, respectively, whereas the blue curve indicates the reflection phase difference. The gray-shaded area in the bottom plot indicates the range of acceptable phase differences.

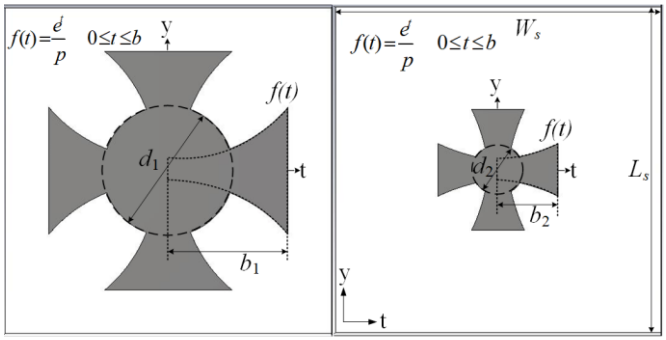

Fig. 11. Geometries of the optimized unit cell designs (upon applying the procedure of Section II-A): Cell 1 (left) and Cell 2 (right).

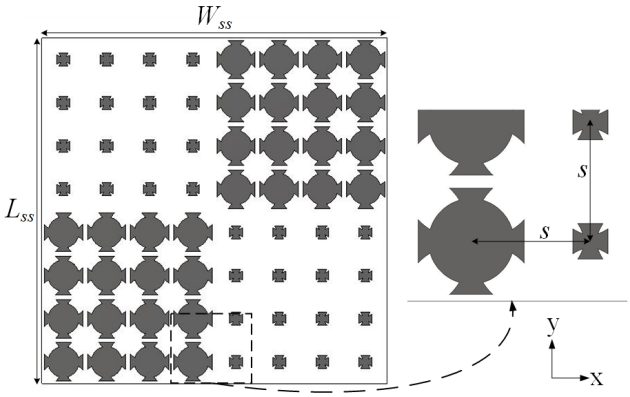

Fig. 13. Geometry configuration of the optimized metasurface (after three-stage optimization procedure).

B. Case 2: Checkerboard Metasurface Applying Mushroom-Like Cell Topologies

The second structure under consideration is more challenging in the sense of being based on more complex unit cell geometries described by a larger number of designable parameters. It is a checkerboard metasurface comprising mushroom-like unit cells; see Figs. 11 and 13. The structure is implemented on a ground-backed Arlon AD250 lossy substrate ($\varepsilon_r = 2.5$, $h = 1.5$ mm, $\tan\delta = 0.0018$). The overall size of a single unit cell is $W_s \times L_s = 6 \times 6$ mm^2. There are three geometrical parameters that determine the shape of each unit cell designs, that is, Cell 1 and Cell 2. Therefore, the two vectors of designable variables are $\boldsymbol{x}_1 = [p_1 b_1\ d_1]^T$ and $\boldsymbol{x}_2 = [p_2 b_2 d_2]^T$; L_s, W_s, L_{ss}, W_{ss}, and s are all fixed. The parameter space $X_1 = X_2 = X$ is determined by the user-defined lower and upper bounds as: $\boldsymbol{l} = [3.5\ 0.3\ 0.2]^T$, $\boldsymbol{u} = [10\ 1.6\ 2.4]^T$; all dimensions are in millimeters. In this case study, the underlying topology of the two unit cells is the same, as opposed to the previous case study, where the two unit cells were based on entirely different structures.

For constructing a metamodel $\boldsymbol{S}$, the training points are arranged in a uniform grid $M_{7.12.7}$ (see Section II-A) with a total of 588 samples in the space X. As mentioned earlier, the underlying topologies of both the cells are identical, and therefore, only a single metamodel is needed. Similarly as for the first example, the accumulated data are divided into the training (85%) and the test data (15%) to be used for split-sample error estimation. The frequency-domain solver of the CST Microwave Studio is used to evaluate the phase reflection responses of the unit cell.

Having a trained metamodel $\boldsymbol{S}$, the concurrent unit cell adjustment is performed (see the procedure of Section II-A) to find a pair of optimum designs. The geometries obtained after completion of the surrogate-assisted global and local optimization are $\boldsymbol{x}_1^* = [4.222,\ 1.600,\ 2.400]^T$ and $\boldsymbol{x}_2^* = [4.944,\ 0.878,\ 0.930]^T$. The designs are shown in Fig. 11, whereas their EM-simulated reflection performance along with the reflection phase difference are presented in Fig. 12. The expected RCS reduction bandwidth that can be deduced from the phase reflection response is from 17 to above 35 GHz.

After finding the optimized pair of unit cells, the checkerboard metasurface is characterized following a similar proce-

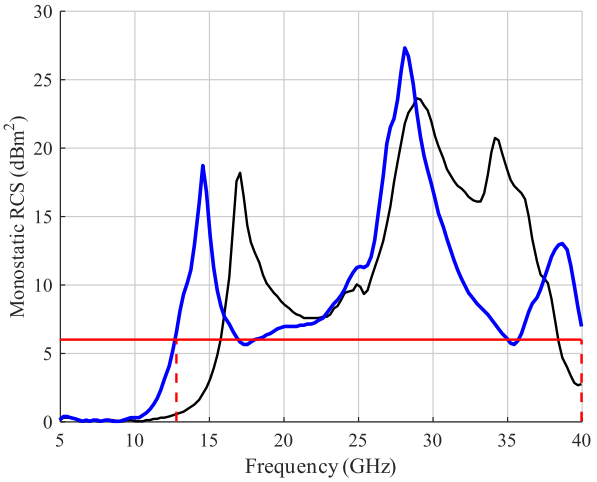

Fig. 14. Monostatic RCS of a metasurface after first and second optimization stages (see Section II-A) (black) and the RCS performance after the final stage (Section II-B) (blue). The horizontal red line represents the 6-dB RCS reduction threshold relative to the PEC surface.

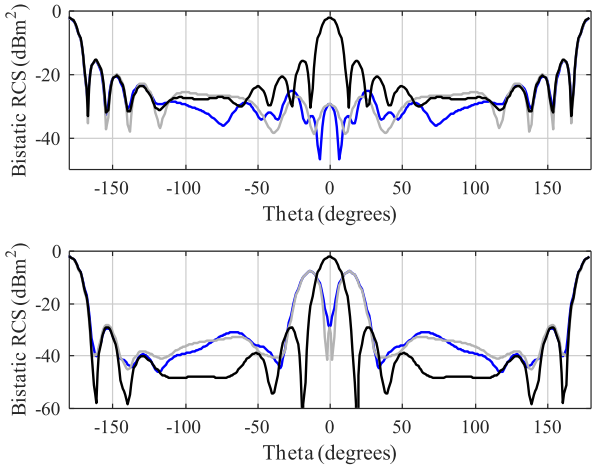

Fig. 15. Bistatic RCS performance at 25 GHz along the principal planes (top) and along the diagonal planes (bottom). The responses at the two planes corresponding to $\varphi = 0/45$ and $\varphi = 90/135$ are marked in blue and gray, respectively, whereas the black curve indicates the scattered field from the PEC surface.

dure as discussed for the first application example. The surface configuration is shown in Fig. 13. The total size of the surface is $W_{ss} \times L_{ss} = 48 \times 48$ mm^2. The interelement spacing of individual unit cells in an array is $s = 6$ mm. The surface is implemented on Arlon AD250 lossy substrate.

Again, the EM-driven local tuning is performed at this stage (see Section II-B). The design obtained at the final optimization stage is $\boldsymbol{x}_A^* = [4.492, 1.601, 4.296, 3.485, 0.795, 0.382]^T$. To quantify the performance of the proposed design framework, the RCS reduction bandwidth obtained when the metasurface is implemented using the cell designs identified by the procedure of Section II-A, and the reduction bandwidth obtained at the final design is demonstrated in Fig. 14.

It can be observed that the machine-learning-based cell optimization procedure already ensures a broadband RCS reduction performance. However, the performance is considerably improved after applying the EM-driven optimization. The 6-dB RCS reduction bandwidth extends from 13 to over 40 GHz. Owing to the implemented acceleration mechanisms, the cost of the final refinement stage is only 32 EM simulations of the metasurface.

In this case, the EM simulation model of the unit cell and the entire surface contains about 22 000, and 2 400 000 mesh cells, respectively. The corresponding simulation times are 70 s and 30 min, respectively. The CPU time required for training data acquisition is about 11 h, whereas the time required for the refinement stage is about 15 h. Consequently, the overall CPU time of the entire design optimization procedure is about 26 h.

Finally, the scattered field as a function of the elevation angle theta θ along the principal and the diagonal planes are presented in Fig. 15. The bistatic RCS performance of the metasurface is compared with the PEC surface of similar size. The results indicate that the metasurface offers nearly 20-dB RCS reduction in both the principal and the diagonal planes.

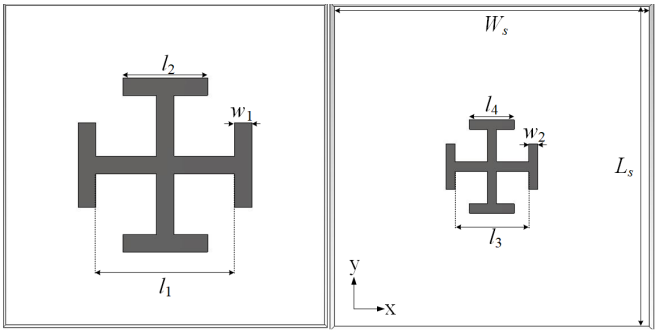

Fig. 16. Geometries of the optimized unit cell designs (as reported in [17]): Cell 1 (left) and Cell 2 (right).

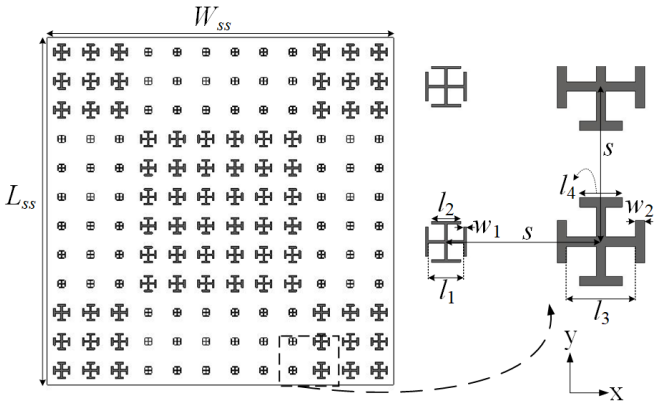

Fig. 17. Geometry configuration of the optimized metasurface (obtained using the optimization procedure of Section II-B).

C. Case 3: Metasurface Using Jerusalem Cross-Shaped Unit Cells

The final application example is based on a surface presented in [17]. It consists of a Jerusalem-cross-shaped unit cell topology. The unit cell geometries and the entire surface configuration are shown in Figs. 16 and 17, respectively. In

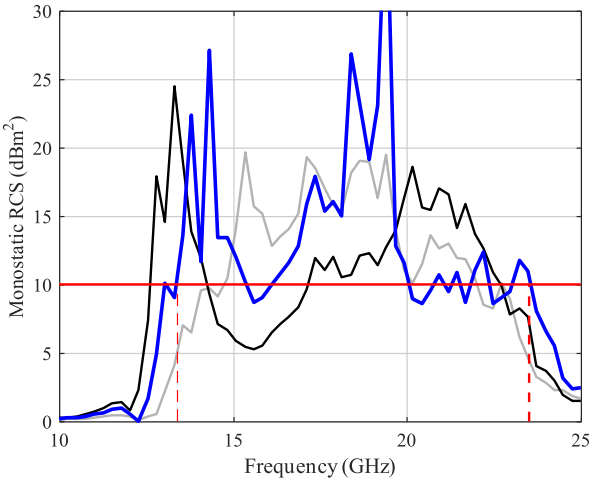

Fig. 18. Monostatic RCS performance of a metasurface design reported in [17] (gray) and after applying the proposed framework of Section II (blue). The horizontal red line represents the 10-dB RCS reduction threshold relative to the PEC surface.

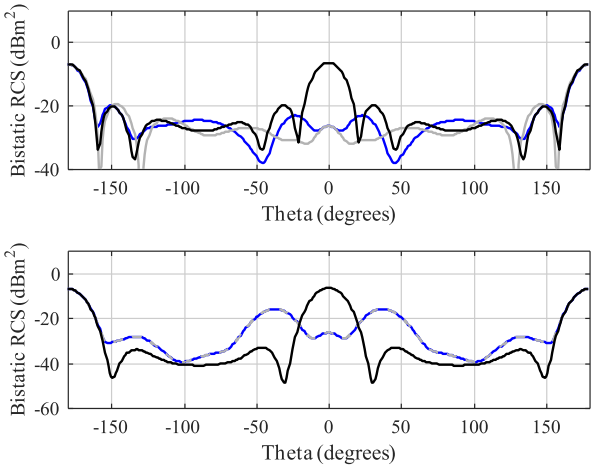

Fig. 19. Bistatic RCS performance at 17 GHz along the principal planes (top) and along the diagonal planes (bottom). The characteristics at the two planes corresponding to $\varphi = 0/45$ and $\varphi = 90/135$ are marked in blue and gray, respectively, whereas the black curve indicates the scattered field from the PEC surface.

this case, a ground-backed Rogers 3010 lossy substrate ($\varepsilon_r = 10.2$, $h = 1.27$ mm, $\tan\delta = 0.0022$) is used to design the individual unit cells and the complete metasurface. The size of a single unit cell is $W_s \times L_s = 4 \times 4$ mm^2. There are three geometrical parameters in both unit cells, and hence the two vectors of designable variables are $\boldsymbol{x}_1 = [l_1 l_2 w_1]^T$ and $\boldsymbol{x}_2 = [l_3 l_4 w_2]^T$; L_s, W_s, L_{ss}, W_{ss}, and s are all fixed. The sample space $X_1 = X_2 = X$ is determined by the lower and upper bounds as: $\boldsymbol{l} = [0.5\ 0.2\ 0.1]^T$, $\boldsymbol{u} = [2\ 1\ 0.3]^T$; all dimensions are in millimeters.

For constructing a surrogate $\boldsymbol{S}$, the training points are arranged in a uniform grid $M_{9.9.7}$ with a total of 567 samples in the space X. Again, the accumulated data are divided into the training (85%) and the test data (15%) to be used for split-sample error estimation. As in the first and second examples, the concurrent unit cell optimization is performed to find a pair of designs. The optimal geometries obtained after completion of the surrogate-assisted global and local optimization are $\boldsymbol{x}_1^* = [0.5408,\ 0.2704,\ 0.1769]^T$ and $\boldsymbol{x}_2^* = [1.9694,\ 0.9847,\ 0.3]^T$.

The checkerboard metasurface is implemented using the optimum unit cell geometries; see Figs. 16 and 17. The overall size of the metasurface is $W_{ss} \times L_{ss} = 48 \times 48$ mm^2, and the intercell spacing is $s = 4$ mm. The EM-driven design optimization procedure is subsequently used in the final design $\boldsymbol{x}_A^* = [0.668,\ 0.716,\ 0.201,\ 1.905,\ 0.902,\ 0.317]^T$. The cost of the final tuning stage is only 56 EM simulations of the metasurface. The monostatic RCS reduction performance as a function of frequency is presented in Fig. 18. As expected, the considerable threshold violations present after the first and the second optimization stages are greatly reduced at the final design.

In this case, the EM simulation model of the unit cell and the entire surface contains about 25 000 (simulation time 75 s) and 1 700 000 mesh cells (simulation time 33 min), respectively. The simulation time required by the training stage is approximately 12 h, and the total time required for entire design optimization procedure to complete is about 42 h.

Notwithstanding, a 10-dB RCS reduction threshold is still slightly violated at certain frequencies. Overall, the RCS bandwidth is extended by about 3 GHz when compared with the design reported in [17].

Fig. 19 shows the bistatic RCS performance versus the elevation angle theta θ along the principal and the diagonal planes. The results imply that the optimized metasurface features more than the 15-dB RCS reduction in the principal and the diagonal planes, compared with the PEC surface.

TABLE I
DESIGN PERFORMANCE AT VARIOUS STAGES OF THE PROPOSED FRAMEWORK

Application Example	Fractional bandwidth (%)		
	Reported in the literature	After two-stage optimization	After EM-driven tuning
Case 1 [23]	61	70	80
Case 2	-	83	>104
Case 3 [17]	39	57*	56

* Fractional bandwidth including level violation at certain frequencies.

D. Discussion

The breakdown of the results obtained at different stages of the proposed design optimization framework is provided in Table I. It can be observed that for the first verification case, the machine-learning-assisted unit cell optimization itself yields 9% enhancement of the fractional RCS reduction bandwidth when compared with the previously reported results, based on the traditional design methods. The EM-driven fine-tuning leads to additional 10% improvement. In the second application example, the improvement is as high as over 21% due to EM-based tuning of the metasurface. Note that the

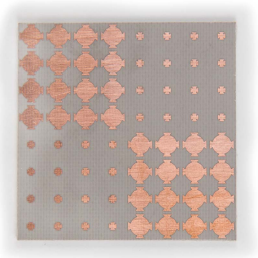

Fig. 20. Photograph of the prototyped checkerboard metasurface.

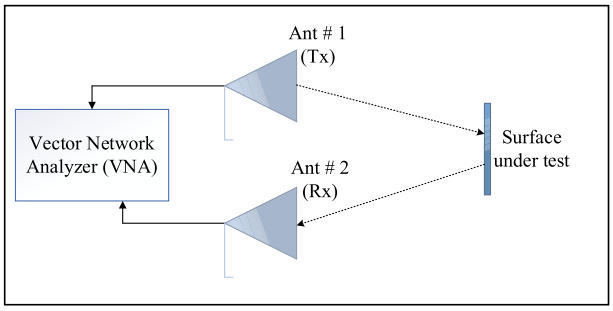

Fig. 21. Block diagram of the measurement environment.

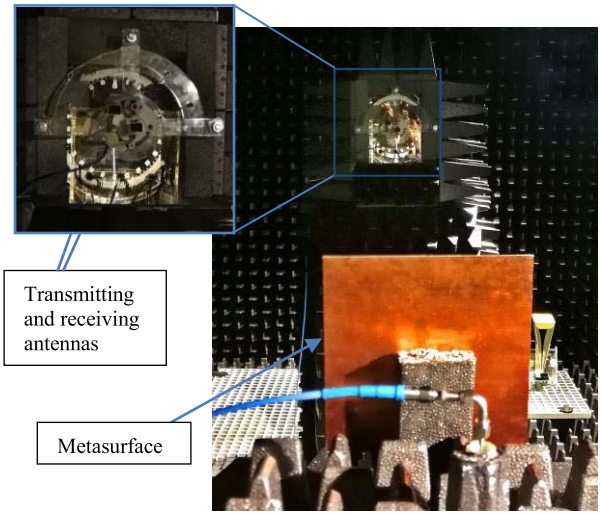

Fig. 22. Measurement setup at Reykjavik University.

absence of any prior work for this geometry only allows us to compare the performance of individual components of our framework. A similar trend has been observed for the third example where application of the proposed algorithmic framework improves the fractional RCS reduction bandwidth from 39% to about 56%. Altogether, it can be concluded that our procedure allows for significant fractional bandwidth enhancements at the level of 15%–25%, when compared with the existing methodologies.

In more general terms, it should be emphasized that the presented design procedure offers several advances over the traditional methods. First, a machine-learning-powered unit cell optimization ensures globally optimum solution within the parameter space which was not previously achievable using experience-driven methods. Having a good initial design upon the accomplishment of the first and the second stages of the algorithm, fine-tuning of the RCS reduction bandwidth through EM-driven optimization can be realized efficiently. It is further accelerated by means of sparse sensitivity updates.

It is worth mentioning that the employment of the regularization term allows for efficient handling of frequency-localized violations, which leads to a seamless improvement of the overall RCS reduction bandwidth, which is not achievable using conventional formulation of the design task. Additionally, our methodology is fully automated. Once the design problem is formulated in a requisite manner, the algorithm successfully finds the best possible design within a realistic timespan and computational resources.

IV. Experimental Setup and Results

In this section, the experimental validation of the metasurface using mushroom-like unit cell designs (see Section III-B) is presented. The monostatic RCS measurement setup is described, and the simulation results are corroborated with the corresponding measurements. Finally, the metasurface performance is benchmarked against the state-of-the-art structures.

A. Measurement Setup and Experimental Validation

The structure described in Section III-*B* has been fabricated to verify the EM simulation results. A photograph of the prototyped metasurface is shown in Fig. 20. The RCS performance of a metasurface has been evaluated in terms of reflectivity, owing to limited amenities. The equivalent PEC surface has been used as a reference to quantify the RCS reduction of a metasurface under consideration.

The measurement setup consists of a vector network analyzer and the two linearly polarized horn antennas (PE9850/2F-15), used as the transmitter and the receiver, respectively. To certify normal incidence of the impinging waves on a structure, the two antennas are place vertically to the surface under test. The distance between the surface and the antennas is maintained to ensure far-field conditions. The schematic of the measurement setup can be found in Fig. 21. The scattering performance of a surface under test is evaluated by the antenna transmission coefficient, captured by the vector network analyzer. In the same way, the reflection from the equivalent PEC surface has been measured for comparison. The measurements have been carried out using the anechoic chamber of Reykjavik University (see Fig. 22).

Fig. 23 presents the simulation and measurement results in a monostatic environment. There are several factors that contribute to the slight disagreement between the two data sets. The misalignment of the transmitting/receiving antenna with respect to surface under test contributes predominantly. Needless to say, proper orientation of a metasurface (realized manually) is a challenging endeavor. A slight misalignment here may lead to fairly large inconsistencies. However, it is evident that the measured RCS reduction follows a similar trend as its simulated counterpart. Additionally, the measured RCS reduction performance agrees to the 6-dB threshold

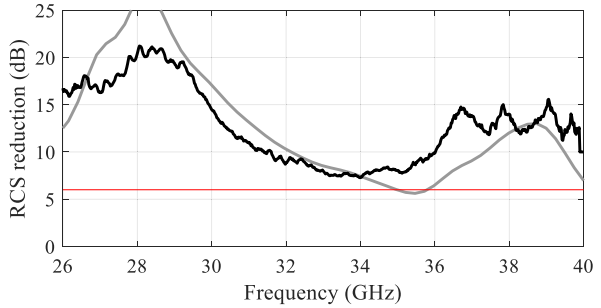

Fig. 23. Measured (black) and simulated (gray) RCS reduction performance comparison. The red curve indicates the 6-dB RCS reduction threshold.

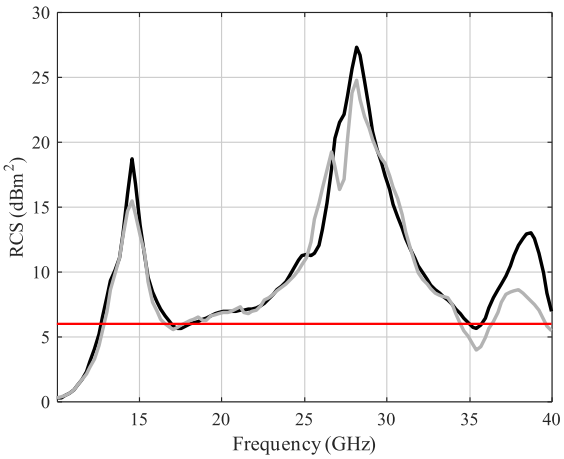

Fig. 24. RCS reduction characteristics of a 2 × 2 (black) and 6 × 6 (gray). The red curve indicates the 6-dB RCS reduction threshold.

in the frequency range of 26.5–40 GHz. The measurement has been limited to over 26.5 GHz due to the available hardware. The above findings allow us to conclude that the designed metasurface features low the scattering property in a broadband frequency range, and therefore, it has the potential to replace the metallic surfaces in applications where high stealthiness is essential.

The primary reason for considering a 2 × 2 metasurface throughout the study is that the RCS reduction performance is always normalized to equivalent size PEC surface, and therefore, the size of the metasurface is a nominal factor. This issue has been discussed in the literature (see [17], [23]). In particular, it has been argued that the RCS reduction performance of a 2 × 2 metasurface with reference to a metallic surface is a decent representative of the corresponding structure of a larger size. This has been numerically corroborated through a comparative study carried out to compare the RCS reduction performance of a 2 × 2 and 6 × 6 metasurface, using the design described in Section III-B. Fig. 24 shows the comparison between these two cases. It can be observed that the RCS reduction responses are well-aligned, which can be viewed as a comparison of the RCS performance invariance with respect to the metasurface size in the considered context.

B. Benchmarking

The main purpose of this article was to propose a systematic framework for computationally efficient and reliable design optimization of low scattering metasurface. In the course of verification of the presented methodology, it has been demonstrated that it does allow for obtaining higher quality designs than those produced by traditional design approaches.

TABLE II
DESIGNED METASURFACE VERSUS STATE-OF-THE-ART DESIGNS

Design	Metasurface size (mm^3)	Frequency range (>6-dB RCS reduction) (GHz)	Fractional bandwidth (%)
[51]	180×180×3.5	8.6–23.4	92
[52]	328×328×3	5.1–7.9	43
[53]	400×400×3.5	5.9–14.1	82
[54]	264×264×3	8.4–23	93
[55]	112×112×6.35	4–10.8	91
[56]	112×112×6.35	3.75–10	90
[24]	150×150×3.175	7.7–16.5	72
[57]	250×250×3.18	9–19.8	75
This work (Section III.*B*)	48×48×1.5	13–40	>104

Here, for the sake of supplementary validation, the metasurface considered in Section III-B is benchmarked against the state-of-the-art designs from the literature to emphasize that our approach is capable of yielding structures that are competitive in terms of relevant performance figures. The latter, for low observable metasurface designs, is primarily the continuous range of frequencies rendering RCS reduction characteristics, when compared with the equivalent metallic surface. For fair assessment, the comparison is carried out in terms of the fractional/relative RCS reduction bandwidth. As indicated in Table II, the presented metasurface design outperforms a number of other reported structures. Additionally, our design covers several radar frequency bands, including Ku, K, and Ka. Consequently, it can be used in a wide selection of applications.

V. CONCLUSION

In this article, we proposed a machine-learning-powered EM-driven design framework to enable the development of high-performance metasurfaces featuring broadband RCS reduction. The latter is particularly desirable in stealth technology, empowering combat aircrafts to potentially evade the enemy's radar to a satisfactory extent. Our framework uses fast metamodels replacing CPU-intensive EM simulations during the initial stages of the design procedure, followed by the expedited EM-driven fine-tuning of the metasurface geometry parameters. Using the surrogate as a fast predictor replacing the EM-simulation model allows us to significantly accelerate the process of determining globally optimal unit cell geometries, that is, maximizing the frequency range for which the required phase difference (here, 180°± 37°) is maintained. The computational cost of the training stage is very much practical (typically, up to a few hours), and it significantly reduces the overall cost of the metasurface design procedure. As a matter of fact, surrogate-assisted approach enables global search, otherwise infeasible when using conventional means.

Subsequently, EM-driven adjustment of the geometry parameters is carried out at the level of the entire metasurface to directly extend the RCS reduction bandwidth. The optimization is realized by applying TR gradient algorithm with sparse sensitivity updates. Furthermore, the objective function for the process is modified by incorporating a regularization term to efficiently handle frequency-localized violations of the RCS reduction threshold. This demonstrably leads to improved reliability and quality of the design process when compared with a conventional formulation of the optimization task.

The design utility of the proposed framework is comprehensively validated using three practical examples, also supported by the experimental validation of a high-performance metasurface involving mushroom-like unit cells. Here, we only considered checkerboard-type metasurfaces; nevertheless, the introduced design optimization methodology is not limited to this particular class of structures. The framework is generic, and it can be applied to any other architecture as long as it is of fixed topology (i.e., the design task can be formulated as the adjustment of geometry/material parameters of the structure). Optimization of the metasurface topology is out of the scope of this work. The overall computational cost of the optimization process typically corresponds to a few dozens of EM simulations of the entire surface at hand, which is remarkably low given that the design process is carried out in a global sense.

The prototyped metasurface has been benchmarked against state-of-the-art designs and demonstrated to be superior in terms of the RCS reduction bandwidth. This further corroborates the efficacy of the proposed algorithmic framework in the development of minimum detectable metasurfaces. The obtained results also reconfirm that optimization of small (2 $\times$ 2) surfaces is sufficient in the considered context (i.e., with the reference to a metallic surface).

The authors believe that the algorithmic procedure proposed in this work can be adopted to design of metamaterials and metasurfaces for other application areas so as to address the challenges specific to the respective fields. These include but are not limited to high-gain antennas, optical filters, radomes, and medical devices.

ACKNOWLEDGMENT

The authors would like to thank Dassault Systemes, France, for making CST Microwave Studio available.

REFERENCES

[1] S. Sun, Q. He, J. Hao, S. Xiao, and L. Zhou, "Electromagnetic metasurfaces: Physics and applications," *Adv. Opt. Photon.*, vol. 11, no. 2, pp. 380–479, 2019.

[2] T. J. Cui, D. R. Smith, and R. Liu, *Metamaterials: Theory, Design, and Applications*. New York, NY, USA: Springer, 2010.

[3] F. Aieta *et al.*, "Aberration-free ultrathin flat lenses and axicons at telecom wavelengths based on plasmonic metasurfaces," *Nano Lett.*, vol. 12, no. 9, pp. 4932–4936, Sep. 2012.

[4] X. Gao, X. Han, W.-P. Cao, H. O. Li, H. F. Ma, and T. J. Cui, "Ultrawideband and high-efficiency linear polarization converter based on double V-shaped metasurface," *IEEE Trans. Antennas Propag.*, vol. 63, no. 8, pp. 3522–3530, Aug. 2015.

[5] F.-C. Huang, C.-N. Chiu, T.-L. Wu, and Y.-P. Chiou, "A circular-ring miniaturized-element metasurface with many good features for frequency selective shielding applications," *IEEE Trans. Electromagn. Compat.*, vol. 57, no. 3, pp. 365–374, Jun. 2015.

[6] M. Paquay, J.-C. Iriarte, I. Ederra, R. Gonzalo, and P. de Maagt, "Thin AMC structure for radar cross-section reduction," *IEEE Trans. Antennas Propag.*, vol. 55, no. 12, pp. 3630–3638, Dec. 2007.

[7] G. A. Rao and S. P. Mahulikar, "Integrated review of stealth technology and its role in airpower," *Aeronaut. J.*, vol. 106, no. 1066, pp. 629–642, Dec. 2002.

[8] T. A. Khan, J. X. Li, Z. Li, M. Abdullah, J. Chen, and A. X. Zhang, "Design of Vivaldi antenna with wideband reduced radar cross section," *AEU Int. J. Electron. Commun.*, vol. 95, pp. 47–51, Oct. 2018.

[9] E. F. Knott, J. F. Schaeffer, and M. T. Michael, *Radar Cross Section*. Rijeka, Croatia: SciTech, 2004.

[10] F. Costa, A. Monorchio, and G. Manara, "Analysis and design of ultra thin electromagnetic absorbers comprising resistively loaded high impedance surfaces," *IEEE Trans. Antennas Propag.*, vol. 58, no. 5, pp. 1551–1558, May 2010.

[11] N. I. Landy, S. Sajuyigbe, J. J. Mock, D. R. Smith, and W. J. Padilla, "Perfect metamaterial absorber," *Phys. Rev. Lett.*, vol. 100, no. 20, pp. 207–402, 2008.

[12] Y. Cheng and H. Yang, "Design simulation and measurement of metamaterial absorber," *J. Appl. Phys.*, vol. 108, 2010, Art. no. 34906.

[13] Y. Ma, Q. Chen, J. Grant, S. C. Saha, A. Khalid, and D. R. S. Cumming, "A terahertz polarization insensitive dual band metamaterial absorber," *Opt. Lett.*, vol. 36, no. 6, pp. 945–947, 2011.

[14] Y. Liu and X. Zhao, "Perfect absorber metamaterial for designing low-RCS patch antenna," *IEEE Antennas Wireless Propag. Lett.*, vol. 13, pp. 1473–1476, 2014.

[15] K. Chang, "Electromagnetic gradient surface and its application to flat reflector antennas," Ph. D. dissertation, Dept. Elect. Electron. Eng., Yonsei Univ., Seoul, South Korea, 2009.

[16] H. P. Seo, Y. S. Kim, Y. Lim, and Y. J. Yoon, "Improving phase continuity in electromagnetic gradient surface for large reflecting structures," in *Proc. IEEE Int. Symp. Antennas Propag.*, Jul. 2012, pp. 1–2.

[17] J. C. Iriarte Galarregui, A. Tellechea Pereda, J. L. M. de Falcon, I. Ederra, R. Gonzalo, and P. de Maagt, "Broadband radar cross-section reduction using AMC technology," *IEEE Trans. Antennas Propag.*, vol. 61, no. 12, pp. 6136–6143, Dec. 2013.

[18] J. C. Iriarte, I. Ederra, R. Gonzalo, and P. de Maagt, "Dual band RCS reduction using planar technology by combining AMC structures," in *Proc. 3rd Eur. Conf. Antennas Propag.*, Mar. 2009, pp. 3708–3709.

[19] M. E. de Cos, Y. Alvarez-Lopez, and F. Las Heras Andres, "On the influence of coupling AMC resonances for RCS reduction in the SHF band," *Prog. Electromagn. Res.*, vol. 117, pp. 103–119, 2011.

[20] M. E. de Cos, Y. Á. Lvarez, and F. Las-Heras, "RCS reduction using a combination of artificial magnetic conductors," in *Proc. 5th Eur. Conf. Antennas Propag. (EUCAP)*, Apr. 2011, pp. 1336–1340.

[21] J. C. Iriarte *et al.*, "Broadband RCS reduction using AMC technology," in *Proc. 5th Eur. Conf. Antennas Propag. (EUCAP)*, Apr. 2011, pp. 1322–1323.

[22] Y. Fu, Y. Li, and N. Yuan, "Wideband composite AMC surfaces for RCS reduction," *Microw. Opt. Technol. Lett.*, vol. 53, no. 4, pp. 712–715, Apr. 2011.

[23] W. Chen, C. A. Balanis, and C. R. Birtcher, "Checkerboard EBG surfaces for wideband radar cross section reduction," *IEEE Trans. Antennas Propag.*, vol. 63, no. 6, pp. 2636–2645, Jun. 2015.

[24] S. H. Kim and Y. J. Yoon, "Wideband radar cross-section reduction on checkerboard metasurfaces with surface wave suppression," *IEEE Antennas Wireless Propag. Lett.*, vol. 18, no. 5, pp. 896–900, May 2019.

[25] T. Han, X.-Y. Cao, J. Gao, Y.-L. Zhao, and Y. Zhao, "A coding metasurface with properties of absorption and diffusion for RCS reduction," *Prog. Electromagn. Res. C*, vol. 75, pp. 181–191, 2017.

[26] F. Costa, A. Monorchio, and G. Manara, "Wideband scattering diffusion by using diffraction of periodic surfaces and optimized unit cell geometries," *Sci. Rep.*, vol. 6, no. 1, Jul. 2016, Art. no. 25458.

[27] Y. Zhao *et al.*, "Broadband diffusion metasurface based on a single anisotropic element and optimized by the simulated annealing algorithm," *Sci. Rep.*, vol. 6, no. 1, Jul. 2016, Art. no. 23896.

[28] A. Edalati and K. Sarabandi, "Wideband, wide angle, polarization independent RCS reduction using nonabsorptive miniaturized-element frequency selective surfaces," *IEEE Trans. Antennas Propag.*, vol. 62, no. 2, pp. 747–754, Feb. 2014.

[29] Y.-C. Hou, W.-J. Liao, C.-C. Tsai, and S.-H. Chen, "Planar multilayer structure for broadband broad-angle RCS reduction," *IEEE Trans. Antennas Propag.*, vol. 64, no. 5, pp. 1859–1867, May 2016.

[30] H. Yang *et al.*, "A programmable metasurface with dynamic polarization, scattering and focusing control," *Sci. Rep.*, vol. 6, no. 1, Dec. 2016, Art. no. 35692.

[31] M. Chen, M. Kim, A. M. H. Wong, and G. V. Eleftheriades, "Huygens' metasurfaces from microwaves to optics: A review," *Nanophotonics*, vol. 7, no. 6, pp. 1207–1231, Jun. 2018.
[32] J. Ji, J. Jiang, G. Chen, F. Liu, and Y. Ma, "Research on monostatic and bistatic RCS of cloaking based on coordinate transformation," *Optik*, vol. 165, pp. 117–123, Jul. 2018.
[33] S. Sui *et al.*, "Absorptive coding metasurface for further radar cross section reduction," *J. Phys. D, Appl. Phys.*, vol. 51, no. 6, Feb. 2018, Art. no. 065603.
[34] S. Koziel and A. Pietrenko-Dabrowska, "Efficient gradient-based algorithm with numerical derivatives for expedited optimization of multi-parameter miniaturized impedance matching transformers," *Radioengineering*, vol. 27, no. 3, pp. 572–578, Sep. 2019.
[35] X. Lin *et al.*, "All-optical machine learning using diffractive deep neural networks," *Science*, vol. 361, no. 6406, pp. 1004–1008, Sep. 2018.
[36] A. D. Tranter *et al.*, "Multiparameter optimisation of a magneto-optical trap using deep learning," *Nature Commun.*, vol. 9, Oct. 2018, Art. no. 4360.
[37] J. Peurifoy *et al.*, "Nanophotonic particle simulation and inverse design using artificial neural networks," *Sci. Adv.*, vol. 4, no. 6, Jun. 2018, Art. no. eaar4206.
[38] X. Chen, W. Xue, H. Shi, L. Wang, S. Zhu, and A. Zhang, "Improving field uniformity using source stirring with orbital angular momentum modes in a reverberation chamber," *IEEE Microw. Wireless Compon. Lett.*, vol. 29, no. 8, pp. 560–562, Aug. 2019.
[39] X. Chen, W. Xue, H. Shi, J. Yi, and W. E. I. Sha, "Orbital angular momentum multiplexing in highly reverberant environments," *IEEE Microw. Wireless Compon. Lett.*, vol. 30, no. 1, pp. 112–115, Jan. 2020.
[40] T. W. Simpson, J. D. Poplinski, P. N. Koch, and J. K. Allen, "Metamodels for computer-based engineering design: Survey and recommendations," *Eng. Comput.*, vol. 17, no. 2, pp. 129–150, Jul. 2001.
[41] S. Koziel, L. Leifsson, and X. S. Yang, "Surrogate-based optimization," in *Simulation-Driven Design Optimization and Modeling for Microwave Engineering*, S. Koziel, X. S. Yang, and Q. J. Zhang, Eds. London, U.K.: Imperial College Press, 2012, pp. 41–80.
[42] S. Koziel and J. W. Bandler, "Reliable microwave modeling by means of variable-fidelity response features," *IEEE Trans. Microw. Theory Techn.*, vol. 63, no. 12, pp. 4247–4254, Dec. 2015.
[43] S. Koziel and A. Pietrenko-Dabrowska, *Performance-Driven Surrogate Modeling of High-Frequency Structures*. New York, NY, USA: Springer, 2020.
[44] F. Feng *et al.*, "Multifeature-assisted neuro-transfer function surrogate-based EM optimization exploiting trust-region algorithms for microwave filter design," *IEEE Trans. Microw. Theory Techn.*, vol. 68, no. 2, pp. 531–542, Feb. 2020.
[45] S. Koziel and A. Pietrenko-Dabrowska, "Expedited optimization of antenna input characteristics with adaptive broyden updates," *Eng. Comput.*, vol. 37, no. 3, pp. 851–862, Sep. 2019.
[46] J. Jiang and J. A. Fan, "Simulator-based training of generative neural networks for the inverse design of metasurfaces," *Nanophotonics*, vol. 9, no. 5, pp. 1059–1069, Nov. 2019.
[47] W. Ma, F. Cheng, Y. Xu, Q. Wen, and Y. Liu, "Probabilistic representation and inverse design of metamaterials based on a deep generative model with semi-supervised learning strategy," *Adv. Mater.*, vol. 31, no. 35, Aug. 2019, Art. no. 1901111.
[48] A. Hoorfar, "Evolutionary programming in electromagnetic optimization: A review," *IEEE Trans. Antennas Propag.*, vol. 55, no. 3, pp. 523–537, Mar. 2007.
[49] A. R. Conn, N. I. M. Gould, and P. L. Toint, *Trust Region Methods* (MPS-SIAM Series on Optimization). Philadelphia, PA, USA: Society for Industrial and Applied Mathematics, 2000.
[50] S. Koziel, J. W. Bandler, and Q. S. Cheng, "Robust trust-region space-mapping algorithms for microwave design optimization," *IEEE Trans. Microw. Theory Techn.*, vol. 58, no. 8, pp. 2166–2174, Aug. 2010.
[51] S. H. Esmaeli and S. H. Sedighy, "Wideband radar cross-section reduction by AMC," *Electron. Lett.*, vol. 52, no. 1, pp. 70–71, Jan. 2016.
[52] X. Liu, J. Gao, L. Xu, X. Cao, Y. Zhao, and S. Li, "A coding diffuse metasurface for RCS reduction," *IEEE Antennas Wireless Propag. Lett.*, vol. 16, pp. 724–727, 2017.
[53] J. Yang, Y. Cheng, C. Ge, and R. Gong, "Broadband polarization conversion metasurface based on metal cut-wire structure for radar cross section reduction," *Materials*, vol. 11, no. 4, p. 626, Apr. 2018.
[54] L. Ali, Q. Li, T. A. Khan, J. Yi, and X. Chen, "Wideband RCS reduction using coding diffusion metasurface," *Materials*, vol. 12, no. 17, p. 2708, Aug. 2019.
[55] W. Chen, C. A. Balanis, and C. R. Birtcher, "Dual wide-band checkerboard surfaces for radar cross section reduction," *IEEE Trans. Antennas Propag.*, vol. 64, no. 9, pp. 4133–4138, Sep. 2016.
[56] A. Y. Modi, C. A. Balanis, C. R. Birtcher, and H. N. Shaman, "Novel design of ultrabroadband radar cross section reduction surfaces using artificial magnetic conductors," *IEEE Trans. Antennas Propag.*, vol. 65, no. 10, pp. 5406–5417, Oct. 2017.
[57] Q. Zheng *et al.*, "Wideband, wide-angle coding phase gradient metasurfaces based on pancharatnam-berry phase," *Sci. Rep.*, vol. 7, no. 1, Apr. 2017, Art. no. 43543.
[58] Y. Zhuang, G. Wang, J. Liang, T. Cai, W. Guo, and Q. Zhang, "Flexible and polarization-controllable diffusion metasurface with optical transparency," *J. Phys. D, Appl. Phys.*, vol. 50, no. 46, Nov. 2017, Art. no. 465102.

Slawomir Koziel (Senior Member, IEEE) received the M.Sc. and Ph.D. degrees in electronic engineering from the Gdansk University of Technology, Gdansk, Poland, in 1995 and 2000, respectively, and the M.Sc. degrees in theoretical physics and in mathematics and the Ph.D. degree in mathematics from the University of Gdansk, Gdansk.

He is currently a Professor with the Department of Engineering, Reykjavik University, Reykjavik, Iceland. His research interests include CAD and modeling of microwave and antenna structures, simulation-driven design, surrogate-based optimization, space mapping, circuit theory, analog signal processing, evolutionary computation, and numerical analysis.

Muhammad Abdullah received the B.Sc. degree from the University of Engineering and Technology, Lahore, Pakistan, in 2016, and the M.Sc. degree from Xi'an Jiaotong University (XJTU), Xi'an, China, in 2019.

Since late 2019, he has been associated with the Department of Engineering, Reykjavik University, Reykjavik, Iceland, as a Researcher. From 2018 to 2019, he was with the Electromagnetics and Communication Laboratory, XJTU. On completion of M.Sc. degree, he received the excellent master's thesis award. His broader research interests include surrogate-based modeling and optimization, CAD and modeling of antennas and other high-frequency structures, simulation-driven design, machine-learning techniques, and millimeter-wave communication.